JOURNAL OF MASS SPECTROMETRY, VOL. 32, 577–592 (1997)

SPECIAL FEATURE: TUTORIAL

Ion Mobility Measurements and their Applications to Clusters and Biomolecules

David E. Clemmer
Department of Chemistry, University of Indiana, Bloomington, IN 47405, USA

Martin F. Jarrold
Department of Chemistry, Northwestern University, 2145 Sheridan Road, Evanston, IL 60208, USA

Ion mobility measurements can be used to obtain structural information for large polyatomic ions in the gas phase. The methods are flexible and can be applied to a wide range of chemical systems. This article reviews the development of these methods and discusses recent applications to complex ions such as atomic clusters and large biomolecules.

J. Mass Spectrosc. **32**, 577–592 (1997)
No. of Figs: 15 No. of Tables: 1 No. of Refs: 111

KEYWORDS: ion mobility measurements; poyatomic ions; atomic clusters; large biomolecules

INTRODUCTION

In this article we describe some of the recent work that has been performed using ion mobility measurements to deduce structural information for polyatomic ions. Determining the structure of a polyatomic ion in the gas phase is a challenging problem, that is usually approached by indirect methods such as dissociation or reactivity studies. Ion mobility measurements have recently emerged as a technique that can provide more direct information about the geometries of large polyatomic ions. The structural information obtained from these studies is not as detailed as information from high-resolution spectroscopic studies, but in many cases the types of spectroscopic studies needed to provide structural information cannot be applied to polyatomic ions in the gas phase. While the use of ion mobility measurements to deduce structural information has grown in the last five years, both the experimental techniques and theoretical methods employed in these studies were largely developed over two decades ago.

The mobility of a gas-phase ion is a measure of how rapidly it moves through a buffer gas under the influence of an electric field. Mobility measurements are performed in a drift tube, which contains the buffer gas and usually has a series of electrodes to provide a uniform electric field. The electric field accelerates the ions, while collisions with the buffer gas decelerate them, leading to a constant drift velocity, v_D. The mobility, K, is the ratio of the drift velocity to the electric field, $K = v_D/E$, and it contains information about the interaction between the ion and the buffer gas. For atomic ions, the mobility depends on the electronic state, as shown by Rowe *et al.*[1] in 1980. For a large polyatomic ion, the mobility depends on the average collision cross-section. An ion with a large average cross-section undergoes more collisions with the buffer gas and travels more slowly than an ion with a small average collision cross-section. Thus mobility measurements can be used to separate ions with different geometries. For example, Hagen[2] demonstrated in 1979 that structural isomers of polycyclic aromatic hydrocarbons could be separated by their different mobilities. This separation provides the basis for a sensitive and selective analytical technique, ion mobility spectrometry,[3,4] developed by Cohen and Karasek in 1970.

Ion mobility spectrometry, or 'plasma chromatography' as it was first called, uses mobility rather than mass to separate ions. It has been used to detect drugs, chemical warfare agents, explosives and environmental pollutants.[5,6] Several groups have used mobility measurements to characterize the size distribution of aerosol particles and small metal particles.[7,8] In addition to information about ion mobilities, drift tube studies can provide information about ion–molecule reaction kinetics and equilibria. The injected-ion drift tube technique, where mass-selected ions are injected into the drift tube from an external source, was developed by Hasted and co-workers[9] in 1966. This technique has been used by many different groups, including

Correspondence to: D. E. Clemmer.
Contract grant sponsor: National Science Foundation; Contract grant number: CHE-9306900; Contract grant number: CHE-9625199; Contract grant number: CHE-97XXXXX.
Contract grant sponsor: Petroleum research Fund.

CCC 1076–5174/97/060577–16 $17.50

Received 10 April 1997
Accepted 11 April 1997

those of Warneck, Burke, Lindinger, Johnsen and Biondi and Arnold and co-workers, to measure mobilities and study ion chemistry.[10–15] The main focus of the early work employing this technique was to measure mobilities and study ion–molecule reactions important in understanding the chemistry of the upper atmosphere. An advantage of the injected ion drift tube technique is that it can be used with a wide variety of sources. The early work employed simple electron impact sources. More recently, Jarrold and co-workers[16,17] coupled a pulsed laser vaporization source to an injected ion drift tube apparatus and used it to study the chemistry of mass-selected cluster ions, focusing on silicon clusters. Bowers and co-workers[18] subsequently used a similar approach to study the chemistry of metal cluster ions and to measure the mobilities of atomic metal ions. They found large differences in the mobilities of metal ions in different electronic states. In 1991, this group reported ion mobility measurements for carbon cluster ions showing that different structural isomers could be resolved.[20] This work was timely, because of the enormous interest in fullerenes and carbon clusters at that time and remarkable because of the large number of isomers that were resolved. Obtaining structural information for gas phase atomic clusters is a particularly challenging problem and in addition to carbon clusters,[20–23] ion mobility measurements have been used to study silicon clusters, germanium clusters, aluminum clusters and a variety of metal-containing carbon clusters. Bierbaum and co-workers[30] have recently used mobility measurements to study ion–molecule clusters.

It is possible that ions that are generated in the source are not in their lowest energy geometries. A simple annealing technique makes it possible to use ion mobility measurements to examine the isomerization processes of a polyatomic ion.[31] If the ions are injected into the drift tube at elevated kinetic energies, collisions with the buffer gas lead to a transient heating cycle. While hot, the ions can isomerize and at high injection energies they may fragment. Since the transient heating cycle occurs close to the entrance of the drift tube, the rest of the drift tube can be used to probe the geometries of the annealed parent ion or the fragments. This approach has been used to provide important information about isomerization processes in carbon clusters and the mechanism of fullerene formation.[32,33]

While covalently bound clusters, particularly carbon clusters, have isomers with very different shapes and hence very different mobilities, metal clusters, ionic clusters and other polyatomic ions generally have isomers with similar shapes. The application of ion mobility measurements to these species is hindered by the low resolution available in injected ion drift tube experiments. To overcome this problem, Dugourd *et al.*[34] have recently constructed a high-resolution ion mobility apparatus with a resolving power over a order of magnitude better than available from the previous injected ion drift tube experiments. In order to achieve the higher resolving power, it is necessary to operate with much stronger drift fields and higher buffer gas pressures. The resulting experimental configuration has much in common with the ion mobility spectrometers developed for analytical applications in the 1970s. With the increased resolving power, many more structural isomers have been resolved, even for carbon clusters.

Another exciting development is the recent application of ion mobility methods to examine the conformations of peptides and proteins in the gas phase. Since the development of suitable ionization methods,[35–37] there has been interest in examining the geometries of large biological molecules in the gas phase.[38–47] Several groups have previously performed ion mobility measurements for biological molecules,[48–50] although no effort was made to deduce structural information in this work. Bowers and co-workers[51–53] have recently reported ion mobility measurements for the peptide bradykinin. The bradykinin ions for this study were produced by matrix-assisted laser desorption/ionization (MALDI).[37] Only one structure was resolved and the cross-sections deduced from the mobilities were essentially independent of temperature. Extensive molecular dynamics studies were performed and suggested that the gas-phase structure of this peptide is dominated by an intramolecular 'solvation' shell around the charge.[53] Clemmer, Jarrold and co-workers have performed a series of ion mobility measurements for protein ions produced by electrospray ionization. Electrospray ionization generates protein ions in a distribution of charge states,[54] so that ion mobility measurements can be performed as a function of the charge. Measurements have now been performed for cytochrome *c*,[55–58] bovine pancreatic trypsin inhibitor (BPTI),[57] apomyoglobin,[59] lysozyme[60] and ubiquitin,[61] and many different conformations have been resolved. In addition, the 'denaturation' and refolding of these gas-phase proteins has been examined using collisional heating and proton stripping reactions to manipulate the charge state.

EXPERIMENTAL CONSIDERATIONS

Mobilities are measured by determining the amount of time it takes for a short packet of ions to travel through the drift tube. Since the mobility depends on the buffer gas number density, reduced mobilities, scaled to the number density at STP, are usually reported. The reduced mobility is given by

$$K_0 = \frac{L^2}{t_D V} \times \frac{273.2}{T} \times \frac{p}{760} \quad (1)$$

where V is the voltage drop across the drift tube, L is its length, t_D is the drift time, p is the buffer gas pressure in Torr (1 Torr = 133.3 Pa) and T is the temperature of the buffer gas. Since all the parameters in Eqn (1) can be determined with an accuracy of better than 1%, it is not difficult to obtain an absolute accuracy of a few percent in ion mobility measurements and a reproducibility of better than 1%. The parameter that determines an ion's energy in a drift tube is the ratio of the electric field to the buffer gas number density, E/N. At low E/N, where the drift velocity is small compared with thermal velocities, the mobility is independent of the field strength. This is called the low-field limit. In the high-field limit, where the drift velocity is much larger than thermal velocities, the mobility depends on E/N and the ions may align to some extent in the drift tube.[62] Ion mobil-

ity measurements that are designed to deduce structural information should usually be performed in the low-field regime.

If a short packet of ions is injected into the drift tube, the flux of ions leaving the drift tube as a function of time can be calculated from the transport equation.[63] For a single isomer the drift time distribution is given by

$$F(t) = \int dt_p P(t_p) \frac{C[v_D + L/(t - t_p)]}{(DT)^{1/2}} \times \left\{1 - \exp\left[\frac{-r_0^2}{4D(t - t_p)}\right]\right\} \exp\left\{\frac{-[L - v_D(t - t_p)]^2}{4D(t - t_p)}\right\} \quad (2)$$

where v_D is the drift velocity, r_0 is the radius of the drift tube entrance aperture, $dt_p P(t_p)$ is the distribution function of the packet of ions entering the drift tube, C is a constant and D is the diffusion constant. Under low-field conditions D is directly proportional to K, $D = Kk_B T/ze$,[63] where ze is the charge on the ion and k_B is Boltzmann's constant. Comparison of the measured distributions with those calculated with Eqn (2) can reveal whether the measured peak consists of more than one isomer. The resolution is limited by diffusion of the ion packet as it travels through the drift tube. If two isomers have mobilities that differ by less than the ion packet expands, they will not be resolved. As described by Revercomb and Mason[64] in 1974, the resolving power is given approximately by

$$\frac{t_D}{\Delta t} = \left(\frac{LEze}{16k_B T \ln 2}\right)^{1/2} \quad (3)$$

It is apparent from this expression that in order to increase the resolving power it is necessary to lower the temperature, increase the drift field or increase the length of the drift tube. Lowering the temperature from 298 to 77 K increases the resolving power by a factor of two. If the drift field is increased there must be a corresponding increase in the buffer gas pressure in order to keep the mobilities in the low-field limit. However, for pressures above around 10 Torr it becomes increasingly difficult to inject intact polyatomic ions into the drift tube from an external source, since they must overcome the buffer gas flowing out of the drift tube. As the buffer gas pressure is increased, higher injection energies are needed to inject the ions, and then they fragment. The length of the drift tube is limited by the expansion of the ion packet by diffusion as it travels through the drift tube. If the drift tube is too long, the ions are lost to the drift tube walls.

The constraints outlined in the preceding paragraph define two basic experimental configurations for performing ion mobility measurements for polyatomic ions:

1. A low-resolution configuration, where ions are injected into the drift tube from an external source. With the buffer gas pressure limited to less than 10 Torr, the drift field is limited to around 10 V cm^{-1} and the drift tube can be up to several tens of centimeters long. The resolving power of this configuration is around 10–20.

2. A high-resolution configuration, where ions are generated in a source attached directly to the drift tube. With a buffer gas pressure of hundreds of Torr, drift fields of hundreds of volts per centimeter can be employed and the drift tube can be up to several meters long. The resolving power of this configuration is around 200–400.

The injected ion drift tube method and the selected ion flow-drift tube developed by Howorka *et al.*[65] fall into the first category. An injected ion drift tube apparatus usually consists of a source to generate the ions, a mass spectrometer to select a particular mass to charge ratio, a drift tube, followed by a second mass spectrometer and ion detector. A wide variety of different sources have recently been employed with this configuration, including pulsed laser vaporization,[16] pulsed laser desorption,[66] MALDI[51] and electrospray ionization.[55] Figure 1 shows a schematic diagram of the recently constructed injected ion drift tube apparatus of Valentine and Clemmer.[58] This apparatus is equipped with an electrospray source. The source has a differentially pumped desolvation region. A base can be added to this region to reduce the charge on the electrosprayed ions through proton stripping reactions. After passing through the desolvation region the ions enter the vacuum chamber. They are then focused into the drift tube. There is no initial mass selection in this apparatus. After passing through the drift tube, the ions are focused into a quadrupole mass spectrometer and then detected by an off-axis collision dynode and dual microchannel plates.

Three features of the injected ion drift tube configuration deserve to be mentioned.

1. *Chemical reactivity/mobility measurements.* A reagent can be introduced into the drift tube to examine the chemical reactivity of the resolved isomers. For

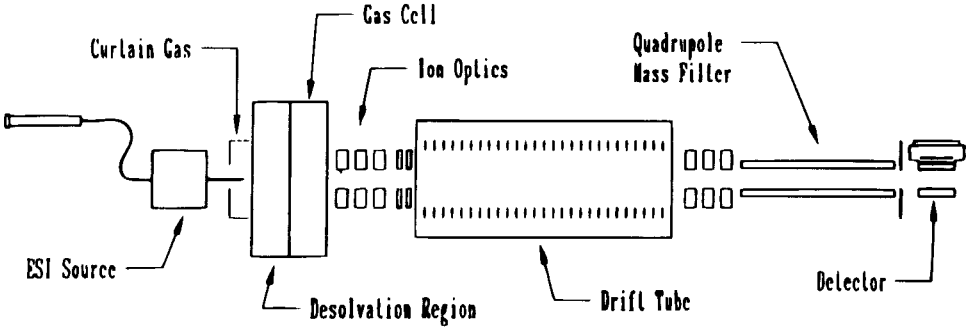

Figure 1. Schematic diagram of injected ion drift tube apparatus at the University of Indiana.

example, this approach has been used to examine the reactivity of silicon clusters in different geometries.[67] Recently, Valentine and Clemmer[58] have used it to examine H–D exchange in cytochrome c.

2. *Collisional annealing and dissociation.* As the ions are injected into the drift tube the injection energy is thermalized by collisions with the buffer gas. During this process some of the injection energy is converted into internal energy, heating the injected ion. After the ion's injection energy is thermalized, and further collisions with the buffer gas remove the ion's excess internal energy. While hot the ions may isomerize or, at high injection energies, fragment. The transient heating and cooling process occurs close to the entrance of the drift tube, so the rest of the drift tube can be used to examine the geometries of any new isomers or fragment ions that are formed. Analysis of the injection energy thresholds can provide information about the activation energies for isomerization or dissociation.

3. *Thermal annealing.* By changing the temperature of the drift tube, isomerization processes can be followed as a function of temperature and the results used to derive activation energies. This approach has been used to follow the isomerization of aluminum clusters[26] and, recently, to study the thermal unfolding of gas-phase proteins.[69]

This wide variety of different ion mobility experiments illustrates the enormous flexibility of the injected ion drift tube approach.

The high-resolution configuration described above employs much higher drift fields. However, because of the high buffer gas pressure, which is necessary to keep the drifting ions in the low-field limit, mass-selected polyatomic ions cannot be injected from an external source. This configuration provides the basis for ion mobility spectrometry, the analytical technique based on the separation of ions by their mobilities. In ion mobility spectrometry, the mobility measurements are performed at atmospheric pressure and the buffer gas is generally nitrogen or air. Ions are usually produced by a radioactive ^{63}Ni source that produces β-particles. A complex series of ion–molecule reactions follows the initial ionization process, ultimately producing analyte product ions. The ions are usually detected at the end of the drift tube by a collector plate and an amplifier. With the high buffer gas pressures employed and because the apparatus is not constructed to high vacuum standards, the formation of large ion–molecule clusters, particularly those involving water, is avoided by heating the drift tube. A variety of ionization techniques have been employed with ion mobility spectrometry including laser desorption[70] and electrospray ionization.[71]

The ion mobility spectrometers that are optimized for analytical applications are not really suitable for studies directed at deriving information about the geometries of polyatomic ions. Dugourd *et al.*[34] have recently described a high-resolution ion mobility apparatus designed for this task. A schematic diagram is shown in Fig. 2. Briefly, the apparatus consists of a source region which is directly coupled to a 63 cm long drift tube. The source region and drift tube contain helium buffer gas at a pressure of $\sim$500 Torr. The ions are generated by pulsed laser vaporization or pulsed laser desorption. After formation, the ions are directed by shaped electric fields to an aperture in the ion gate that separates the source region from the drift tube. A concern with this configuration is that neutral species should not be allowed to diffuse from the source into the drift tube,

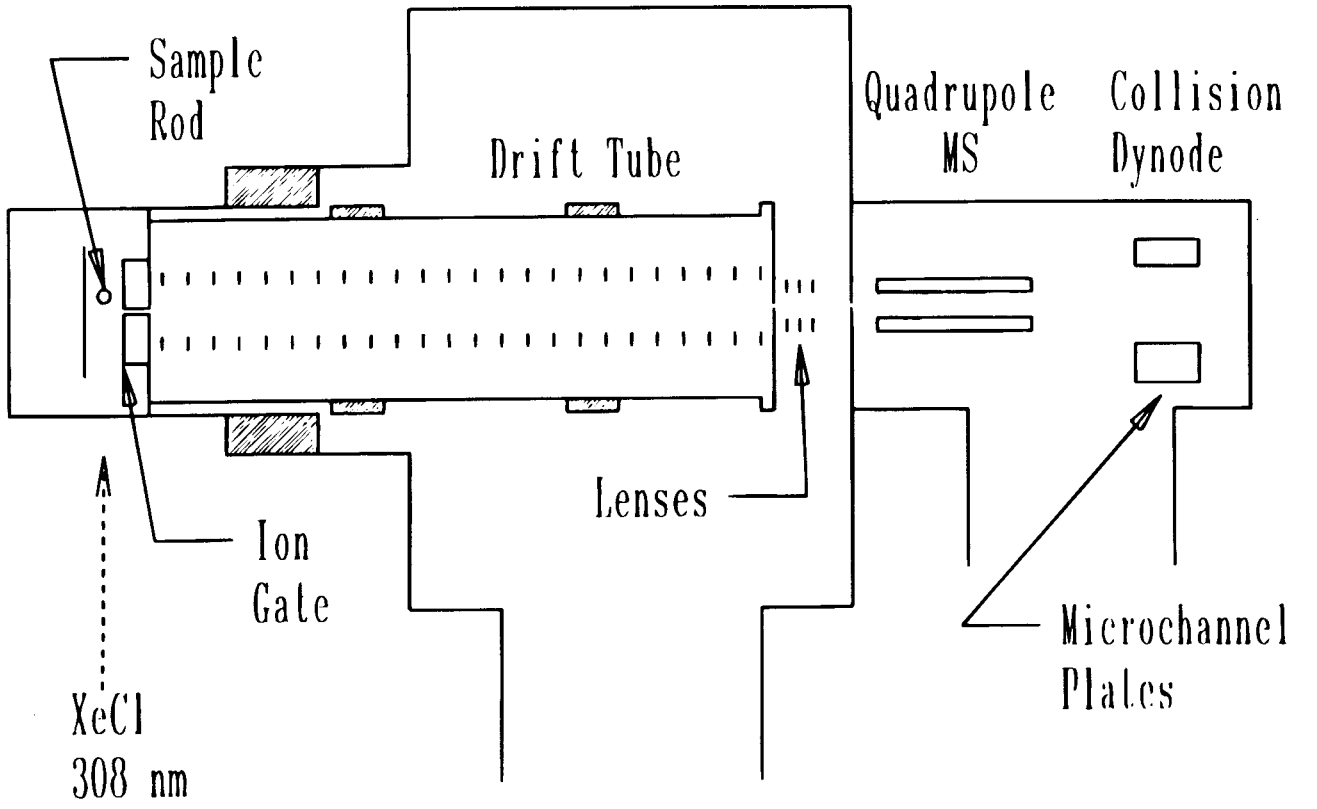

Figure 2. Schematic diagram of the high resolution ion mobility apparatus at Northwestern University.

because charge transfer may then occur in the drift tube and this could distort the measured drift time distributions. The ion gate consists of a 0.5 cm diameter by 2.5 cm long channel with a uniform electric field along its length. A flow of helium buffer gas through the ion gate, from the drift tube into the source region, prevents neutral species from entering the drift tube, while the electric field pulls the ions through the ion gate into the drift tube. The ions then travel along the length of the drift tube under the influence of a uniform electric field generated by a stack of isolated rings and a voltage divider. At the end of the drift tube, some of the ions exit through a small aperture. They are then focused into a quadrupole mass spectrometer and at the end of the quadrupole they are detected. Drift time distributions are recorded with a multichannel scaler using the laser pulse as the start trigger. The drift tube can be heated or cooled so that ion mobility measurements can be performed as a function of temperature.

At the beginning of this section we mentioned that ion mobilities were measured by recording the amount of time it takes for a short packet of ions to travel across the drift tube. This approach is well suited to sources using pulsed lasers, such as laser vaporization, laser desorption and MALDI sources. If the source generates ions continuously a short pulse of ions can easily be generated by an electrostatic shutter. However, the duty cycle is generally less than 1% and discarding 99% of the ions is not a concern if there are enough remaining to perform the mobility measurements in a reasonable time period. This is often not the case. In 1936, Bradbury and Neilsen[72] described another method for measuring drift times that employs two electrostatic shutters at different positions along the length of the drift tube. The same sine wave is applied to both shutters and the signal is recorded as the frequency of the sine wave is swept. Maxima in the transmitted current are observed when the drift time is equal to integral multiples of the half period of the sine wave. The signal recorded as a function of frequency is an interferogram. Hill and co-workers[73] have used Fourier transform techniques to derive the drift time distributions from the interferograms. If two gates are employed, 25% of the ions are utilized rather than 1%. It is also possible to use only a single entrance gate and record both the in phase and out-of-phase signals using a computer, so that 50% of the signal is utilized.

MOBILITY CALCULATIONS

Structural information is obtained from ion mobility measurements by calculating the mobilities for trial geometries and comparing them with the measured values. In the low-field limit, where the measured mobility is independent of the drift field, the mobility is given by[63,75]

$$K = \frac{(18\pi)^{1/2}}{16}\left[\frac{1}{m}+\frac{1}{m_b}\right]^{1/2}\frac{ze}{(k_B T)^{1/2}\Omega_{avg}^{(1,1)}}\frac{1}{N} \quad (4)$$

where m is the mass of the ion, m_b is the mass of a buffer gas atom and $\Omega_{avg}^{(1,1)}$ is the average collision integral or collision cross-section. Assuming that there is no alignment in the drift tube, which is a reasonable assumption for mobilities determined in the low-field limit, then the average collision cross-section can simply be obtained by averaging over all possible collision geometries. Treating the polyatomic ion as a collection of hard spheres, one for each atom, and assuming hard sphere interactions between the ion and buffer gas atom, the average cross-section is obtained by averaging the geometric cross-section over all possible orientations in space. We shall refer to this as the hard sphere projection approximation because the geometric cross-section is simply the area of the shadow cast by the trial geometry in collisions with the buffer gas. This type of model was first used by Mack[76] in 1925. Since computers were not available, Mack mounted a beeswax model of the molecule of interest on a two-axis goniometer so that it could be orientated in any direction. The goniometer was placed between a light source and a graduated screen and the size of the shadow was determined systematically for a variety of orientations. The projection approximation, using computers rather than beeswax models, has been widely used to calculate mobilities of polyatomic ions in the last few years.[21,24,26,29,77–79] Recently, Bowers and co-workers[52] have described an extension of this model that attempts to incorporate long-range interactions in an approximate way so that mobilities can be calculated as a function of temperature. In this model the hard-sphere contact distance is determined from tabulated collision integrals for atom–atom collisions with a 12–6–4 potential, so the model is effectively the projection approximation with a temperature-dependent hard sphere contact distance.

While it is obvious that the hard sphere projection approximation ignores the long-range interactions between the ion and buffer gas, this approach also ignores all the details of the scattering process between the polyatomic ion and buffer gas atom. $\Omega_{avg}^{(1,1)}$ in Eqn (1) is really a collision integral that should be calculated by averaging the momentum transfer cross-section over relative velocity and collision geometry.[63,75] The momentum transfer cross-section depends on the scattering angle, which is the angle between the incoming and outgoing trajectory in a collision between the polyatomic ion and a buffer gas atom. The projection approximation ignores all these details. Shvartsburg and Jarrold[80] have recently described an exact hard spheres scattering model which treats the scattering correctly within the hard sphere limit and they have shown that the projection approximation significantly underestimates the collision integral for some geometries.

The long-range interactions between the buffer gas and the ion should also not be ignored, but accounting for them correctly is not trivial. First an effective potential, consisting of a sum of interactions between the buffer gas atom and all the atoms in the polyatomic ion, must be defined and then trajectories are run within this potential to determine the scattering angles. Many trajectories must be run to average over the impact parameter, the relative velocity and the collision geometry. Calculations along these lines have recently been reported by Mesleh *et al.*,[81] employing a potential consisting of a sum of two-body Lennard–Jones interactions and ion-induced dipole interactions. Table 1

Table 1. Collision integrals calculated for $(C_{60})_2$, $(C_{60})_{13}$, BPTI and cytochrome *c* from trajectory calculations, the exact hard spheres scattering model and the projection approximation[a]

Compound	Cross section (Å²) Trajectory calculations	Exact hard spheres scattering	Projection approximation
$(C_{60})_2$	226 (1.00)	225 (0.99)	216 (0.96)
$(C_{60})_{13}$	813 (1.00)	787 (0.97)	683 (0.84)
BPTI	927 (1.00)	935 (1.01)	767 (0.83)
Cytochrome *c*	1334 (1.00)	1339 (1.00)	1075 (0.81)

[a] The quantities in parentheses show the collision integral divided by the collision integral determined from trajectory calculations.

shows collision integrals calculated for $(C_{60})_2$, icosahedral $(C_{60})_{13}$, BPTI and cytochrome *c* using trajectory calculations, the exact hard spheres scattering model and the projection approximation. The values determined using the projection approximation are up to 20% smaller than those obtained from trajectory calculations. Clearly, the projection approximation is inadequate for calculating the collision integrals of large polyatomic ions. Collision integrals determined from the exact hard spheres scattering model are within a few percent of those obtained from trajectory calculations. This indicates that the main deficiency with the projection approximation is that it ignores the details of the scattering process. The difference between the values determined from the exact hard spheres scattering model and from trajectory calculations result from effects of the long-range potential between the buffer gas atom and the polyatomic ion.

It should be obvious from the preceding discussion that the evaluation of mobilities for comparison with experimental data is not a solved problem. Also, with the recent improvements in resolution, more isomers are being resolved with more subtle structural differences, placing even more stringent demands on the theoretical methods. All the methods described above assume a rigid geometry and inelastic collisions. Lin *et al.*[82] have considered the effects of rotation of the polyatomic ion during a collision with a buffer gas atom. For a helium buffer gas the effect is small. Book *et al.*[78] have reported a study of the effects of vibrational motion on mobilities calculated using the projection approximation. This was done by averaging over an ensemble of geometries generated by molecular dynamics simulations. Bowers and co-workers[52,53] have used a similar approach in their studies of ethylene glycol oligomers and bradykinin. So far, the effects of inelastic collisions have not been considered. A full molecular dynamics treatment is required to examine whether inelastic collisions significantly affect the mobilities. The approach to calculating mobilities described above is based on the belief that it is possible to calculate reliable values from the existing theoretical methods, if the problem is treated with sufficient rigor. Wessel and Jurs[84] employed a different approach to predict mobilities. They used multiple regression analysis and neural networks to predict the mobilities from structural information and a library of measured mobilities. Here the neural network is trained to produce the collision integral from structure–property relationships.

APPLICATIONS

Here we briefly consider some of the recent applications of ion mobility measurements. We will start by describing some work performed on atomic clusters and then review some of the recent studies of biomolecules. The latter focuses mainly on the conformations, unfolding and refolding of multiply charged protein ions in the gas phase.

Carbon and metal-containing carbon clusters

Carbon forms directional covalent bonds in a variety of different bonding configurations. For these reasons, carbon clusters display many different isomeric forms. Some of these isomers, in particular the chains and small monocyclic rings, have been studied for a number of years[85] and much is now known about fullerenes. Ion mobility measurements were first performed for carbon clusters by Bowers and co-workers.[20] Their studies confirmed the existence of chains and monocyclic rings for the smaller clusters and revealed the presence of a several different ring isomers for the larger ones. Figure 3 shows drift time distributions recorded for C_{36}^+ and LaC_{36}^+ produced by laser vaporization of graphite and graphite doped with La_2O_3, respectively. Figure 3(a) and (b) show distributions measured for C_{36}^+ at injection energies of 50 and 225 eV, respectively. The drift time distributions that are recorded at 50 eV and below are independent of injection energy, indicating that the 50 eV distribution reflects the isomer distribution produced by the source. Four distinct peaks are present. These peaks have been assigned to a fullerene at ~600 μs, a graphitic sheet at ~800 μs, bicyclic ring isomers at ~1100 μs and a monocyclic ring at ~1200 μs. It is believed that the bicylic ring is made by clipping together two smaller monocyclic rings. The small shoulder at ~900 μs in Fig. 3(a) is probably due to tricyclic

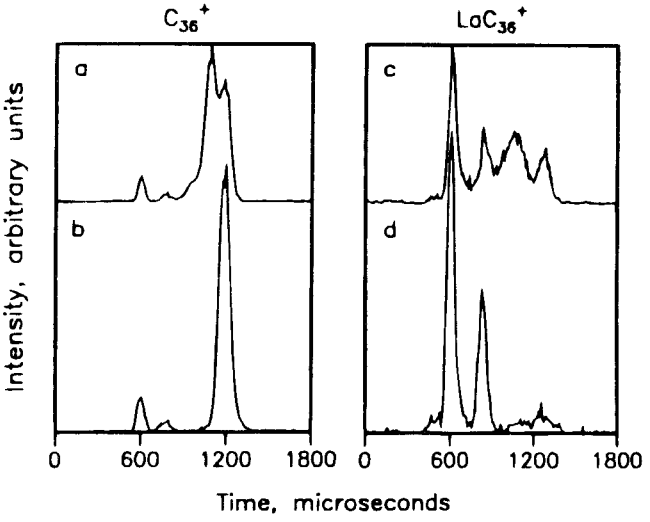

Figure 3. Drift time distributions recorded for (a) and (b) C_{36}^+ and (c) and (d) LaC_{36}^+ at 50 eV (top) and 225 eV (bottom).

rings, which become more abundant for larger clusters. When the injection energy is increased the ions are collisionally heated as they enter the drift tube and the isomer distribution changes. For C_{36}^+ the bicylic and tricylic rings disappear and the abundance of the monocyclic ring increases [compare Fig. 3(a) and (b)]. Isomerization of the bicyclic and tricyclic rings to a monocylic ring is driven by strain relief.[22] The carbon atoms in the rings are sp^1 hybridized and the bicyclic and tricyclic rings are highly strained. It is clear from the results shown in Fig. 3 that the amount of C_{36}^+ fullerene present does not increase significantly as the injection energy is raised. If the injection energy is raised further the monocyclic ring begins to dissociate to smaller ring fragments. Hence small carbon rings do not convert efficiently into fullerenes when collisionally heated. However, for larger clusters the ring isomers do convert into fullerenes. The efficiency of this process increases with increasing cluster size and reaches ~80% for C_{60}^+.[86] These ion mobility and annealing results suggest that the mechanism of fullerene formation involves ring coalescence, followed by isomerization to the fullerene geometry when the rings are large enough.[87]

There has been interest in metallofullerenes since the discovery of fullerenes.[88] Figure 3(c) and (d) show drift time distributions recorded for LaC_{36}^+ with injection energies of 50 and 225 eV, respectively. The same four isomers are present for LaC_{36}^+ as for C_{36}^+, although their relative abundances are different. However, as the injection energy is increased the ring isomers disappear as they convert into an LaC_{36}^+ fullerene and graphite sheet. This does not occur for C_{36}^+, so the metal atom seems to promote the isomerization of the ring isomers into the fullerene and graphite sheet. Careful comparison of the mobilities of the C_{36}^+ and LaC_{36}^+ fullerenes shows that they have almost exactly the same mobilities, which indicates that the metal atom is inside the cage or endohedral for LaC_{36}^+. The metal atom is endohedral for all LaC_n^+ fullerenes with $n > 34$, but smaller LaC_n^+ fullerenes have a non-endohedral metal atom, because the metal atom no longer fits inside the cage. For some metallofullerenes, such as NbC_n^+ fullerenes with an odd number of carbon atoms, the ion mobility measurements indicate that the metal atom is networked into the carbon cage.[27]

Bowers and co-workers[89] have shown that the isomers present for carbon cluster anions are similar to those present for the cations, except the relative abundances are different. For example, the linear chain persists to much larger sizes for the anions, a result that has been attributed to stabilization of the carbene ends of the chain by the extra electrons in the anion. Carbon cluster anions have recently been examined using high-resolution ion mobility methods.[90] Figure 4 shows a high-resolution drift time distribution recorded for C_{24}^-. In this distribution, the feature at 64 ms is due to a linear chain, the three peaks at ~57 ms have drift times close to those expected from previous low-resolution measurements for a monocyclic ring, while the small features at ~50 ms have drift times expected for bicyclic rings. This distribution can be compared with that shown in Fig. 3 for C_{36}^+, where the monocyclic ring at ~1200 μs and bicyclic ring at ~1100 μs are only partially resolved. The existence of several different bicylic ring isomers was anticipated because there are a number of plausible bicyclic ring geometries. However, the presence of several isomers in the monocyclic ring region is a surprise, since there can only be one monocyclic ring. The isomer at ~56 ms appears to be the real monocyclic ring. The geometries of the other isomers are still under investigation.

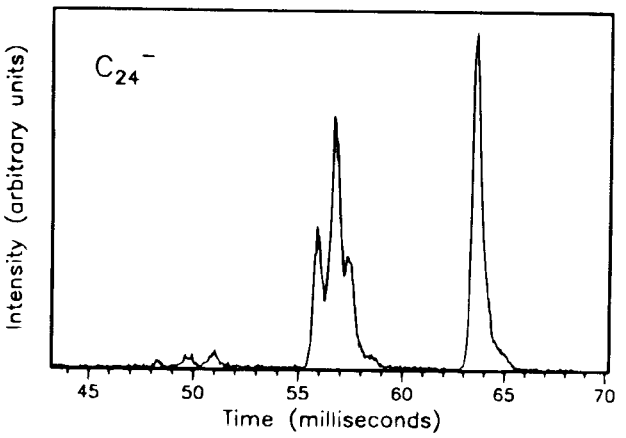

Figure 4. Drift time distribution recorded for C_{24}^- with the high-resolution apparatus. The distribution was recorded with a helium buffer gas pressure of ~500 Torr and a drift voltage of 10 kV.

Sodium chloride nanocrystals

Alkali metal halide clusters are interesting model systems because it appears that they adopt the bulk face-centered cubic (fcc) crystal structure at very small cluster sizes.[91–94] The principle evidence for the bulk-like geometries is the presence of magic number clusters corresponding to complete cuboid geometries. For example, for $(NaCl)_nCl^-$ clusters magic numbers at $(NaCl)_{13}Cl^-$, $(NaCl)_{22}Cl^-$ and $(NaCl)_{37}Cl^-$ have been attributed to completed cuboids with the dimensions 3 × 3 × 3, 5 × 3 × 3 and 5 × 5 × 3. Here, 3 × 3 × 3 means a cube with the dimensions 3 atoms × 3 atoms × 3 atoms, to give a total of 27 atoms, which is the number of atoms in $(NaCl)_{13}Cl^-$. Figure 5 shows the high-resolution drift time distribution measured for the 5 × 5 × 3 magic number cluster, $(NaCl)_{37}Cl^-$. Three features are present in the drift time distribution. These have been assigned by comparing their mobilities to mobilities calculated for geometries optimized using an ionic potential.[95] The middle peak, at 138 ms, has been assigned to the complete 5 × 5 × 3 cuboid, while the other peaks have been attributed to geometries with an incomplete face. The peak at 135 ms has been assigned to an incomplete 5 × 4 × 4 geometry and that at 145 ms to an incomplete 6 × 5 × 3 geometry. The distribution shown in Fig. 5 was recorded with the drift tube at 5 °C. If the drift tube temperature is increased to slightly above room temperature the two features assigned to the incomplete cuboids convert into the complete 5 × 5 × 3 geometry, which indicates that this is the lowest energy geometry.

Figure 6 shows drift time distributions recorded for $(NaCl)_{35}Cl^-$ at 7, 33 and 67 °C. The three isomers present at low temperature have been assigned to an

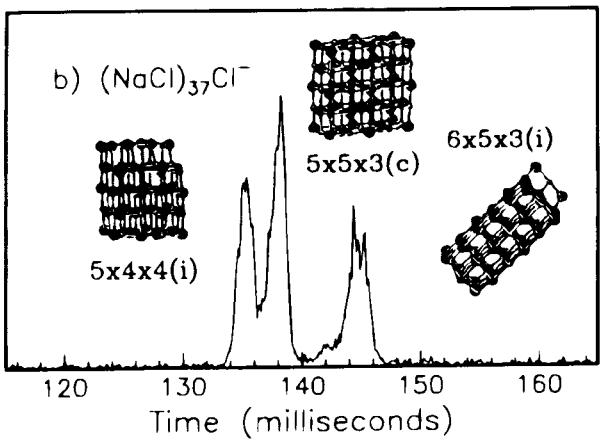

Figure 5. Drift time distribution recorded for $(NaCl)_{37}Cl^-$ with the high-resolution apparatus. The distribution was recorded with a helium buffer gas pressure of ~500 Torr, a drift voltage of 10 kV and a drift tube temperature of 5 °C. The three peaks present have been assigned to an incomplete 5 × 4 × 4, a complete 5 × 5 × 3 and an incomplete 6 × 5 × 3 cuboid geometries. The structures shown in the figure were optimized using an ionic potential.

incomplete 5 × 5 × 3, an incomplete 5 × 4 × 4 and an 8 × 3 × 3 with a single defect. As the temperature is raised the 8 × 3 × 3 and 5 × 3 × 3 isomers convert into the 5 × 4 × 4 geometry. The drift time distribution in Fig. 6 measured at 33 °C shows intensity between the peaks assigned to the 8 × 3 × 3 and 5 × 4 × 4 geometries. This is due to isomerization of the 8 × 3 × 3 to the 5 × 4 × 4 at different places along the length of the drift tube. The amount of time that the ions spend in the drift tube can be varied by varying the drift voltage and the drift time distributions can be analyzed to obtain the isomerization rates.[96] Rate constants have been determined in this way as a function of temperature for a number of the structural transitions in $(NaCl)_nCl^-$ clusters. Arrhenius activation energies for the transitions, determined from the rate constants, are 0.3–0.6 eV. Some of these structural transitions, such as the 8 × 3 × 3 to 5 × 4 × 4 transition of $(NaCl)_{35}Cl^-$, involve the relocation of close to half the atoms in the cluster, so it is remarkable that the activation energies are so low. The low activation energies suggest that the structural transitions occur through a sequence of surface diffusion steps, rather than by a single concerted step.

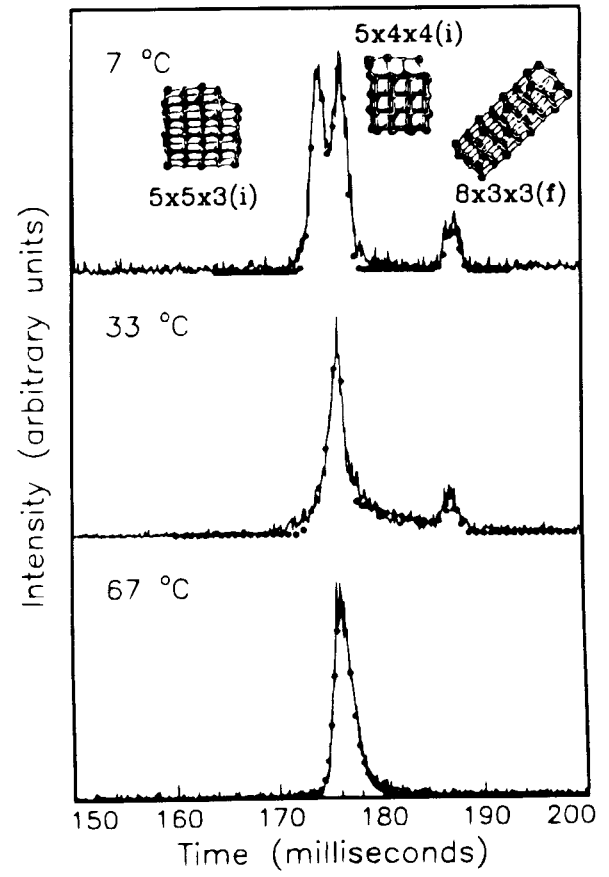

Figure 6. Drift time distributions recorded for $(NaCl)_{35}Cl^-$ at drift tube temperatures of 5, 33 and 67 °C. The three peaks present have been assigned to an incomplete 5 × 5 × 3, an incomplete 5 × 4 × 4 and an incomplete 8 × 3 × 3 cuboid geometries. The structures shown in the figure were optimized using an ionic potential.

Protein ions in the gas phase

Intramolecular interactions, such as hydrogen bonds and van der Waals contacts and solvent interactions, both hydrophobic and hydrophilic, contribute to the free energy of a protein in solution. However, the relative importance of these factors in determining the solution-phase conformation is still the subject of controversy. Studies of unsolvated proteins in the gas phase can provide direct information about their intramolecular interactions. Ion mobility measurements have recently been used to examine the gas-phase conformations of both peptides and proteins. Electrospray ionization produces proteins ions in a distribution of charge states and the charge state distribution depends on the acidity of the solution. Positive ions result mainly from protonation of basic residues while negative ions are produced by deprotonation of acidic residues. Figure 7 shows drift time distributions for the +7 charge state of cytochrome c measured as a function of the injection energy. The distributions are plotted against a reduced time-scale obtained by multiplying the true time-scale by the charge state. This makes it easier to compare distributions measured for different charge states. The ions for these studies were produced by electrospraying an unacidified solution where the protein is in its native form. The dashed line in Fig. 7 shows the drift time expected for the native conformation of cytochrome *c*.[97,98] At low injection energies the peak in the drift time distribution is at slightly shorter times than expected for the native conformation, indicating that the protein is more compact in the gas phase than in solution. In solution, the solvent provides an effective force field which prevents globular proteins from packing tightly. Polar side-chains extend out into the solvent to maximize their interactions and the protein contains cavities large enough to accommodate water molecules. In vacuum, intramolecular interactions make the side-chains collapse on to the protein surface and the protein packs more tightly. According to molecular dynamics simulations, the radius of gyration of BPTI decreases by ~5% on going from solution to vacuum.[99,100] Thus the feature observed at low injec-

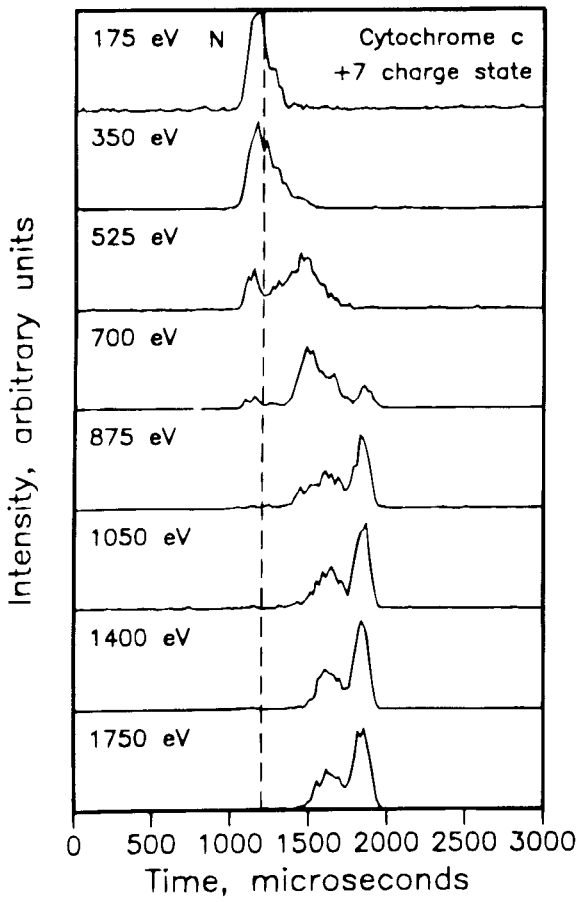

Figure 7. Drift time distributions for the +7 charge state of bovine cytochrome *c* measured as a function of injection energy. The dashed line shows the drift time expected for the native conformation of cytochrome *c*.

tion energy for the +7 charge state of cytochrome c is attributed to contracted or collapsed native conformations. Note that this peak is broader than expected for a single conformation, indicating that a number of conformations with similar mobilities are present. As the injection energy is raised the distribution shifts to longer times and a number of intermediates are resolved at different injection energies. Two peaks remain for injection energies >1050 eV. Clearly the +7 charge state unfolds to less compact conformations when it is collisionally heated. Note that after being collisionally heated, the protein ions rapidly reach thermal equilibrium with the buffer gas because they undergo $>10^5$ collisions cm^{-1} as they travel across the drift tube. However, because of the rapid cooling that occurs, the conformations observed at high injection energies may not be the lowest free-energy conformations at the temperature of the buffer gas.

Cross-sections can be derived directly from the measured drift time distributions using

$$\Omega_{avg}^{(1,1)} = \frac{(18\pi)^{1/2}}{16} \times \frac{ze}{(k_B T)^{1/2}} \left(\frac{1}{m} + \frac{1}{m_b}\right)^{1/2} \times \frac{t_D E}{L} \times \frac{760}{P} \times \frac{T}{273.2} \times \frac{1}{N} \quad (5)$$

Figure 8 shows a plot of the cross-sections of the main features present in the drift time distributions of the +3 to +20 charge states of cytochrome *c*. The +6 to +10 charge states were prepared by electrospraying an unacidified solution. The +11 to +20 charge states were obtained from a solution acidified with 2.5% acetic acid. The lower charge states, +3 to +5, were prepared by adding a base to the desolvation region to reduce the

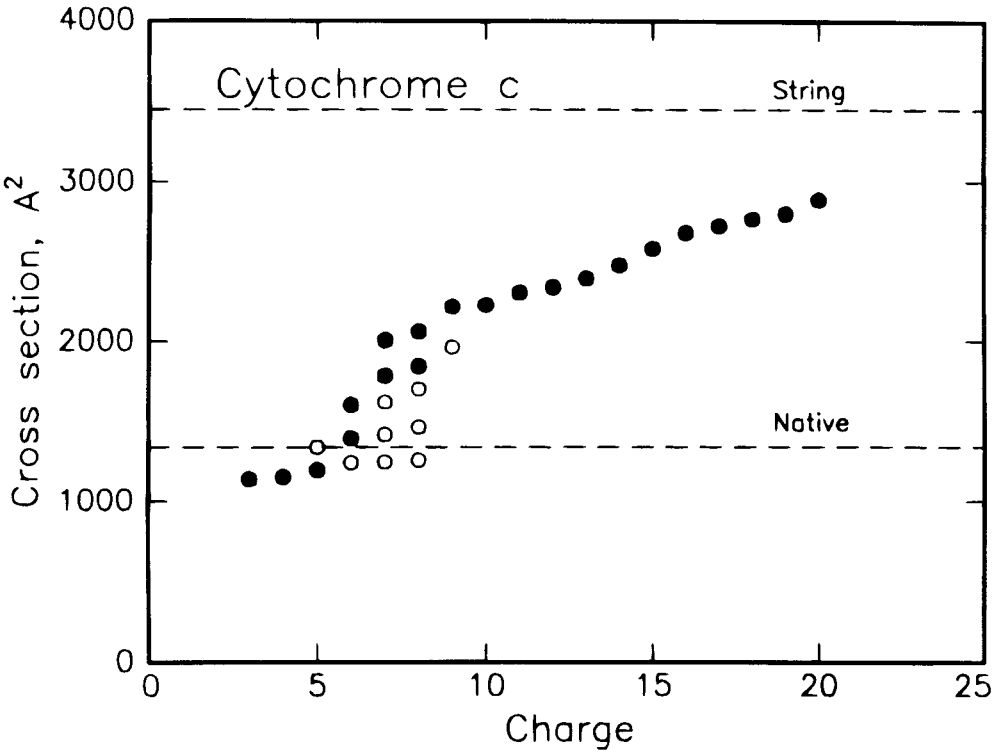

Figure 8. Plot of the collision cross-sections for the main features observed in the drift time distributions for the +3 to +20 charge states of cytochrome *c*. The dashed lines show cross-sections calculated for the native conformation and an extended string.

charge by proton stripping reactions. The filled points in the figure show cross-sections for features observed at high injection energies, while the open points show features observed at lower injection energies. The dashed lines show cross-sections calculated for the native conformation and an extended string obtained by setting most Φ and Ψ angles to 180°. For the low charge states the measured cross-sections are slightly smaller than the cross-section calculated for the native conformation. For the +6 to +8 charge states a structural transition occurs. While conformations, slightly more compact than the native conformation can be prepared for these charge states by electrospraying an unacidified solution, these conformations unfold to less compact ones when collisionally heated. For higher charge states the cross-sections increase with charge and approach the value calculated for the extended string. The unfolding transition that occurs as the charge is increased results from Coulomb repulsion. Intramolecular interactions, hydrogen bonds and van der Waals contacts, hold the protein in a compact, folded conformation. However, as the charge increases, Coulomb repulsion overcomes the attractive intramolecular interactions and the protein unfolds. Coulomb repulsion is more important for proteins in the gas phase than in water, because water has a high dielectric constant.

More information about the stabilities of the observed conformations can be obtained from measurements performed as a function of drift tube temperature.[101] For the +5 charge state only a single feature is observed in the drift time distributions from room temperature up to 300 °C and the cross-section for this feature varies only slightly with temperature. Thus temperatures as high as 300 °C are not enough to unfold the +5 charge state of cytochrome *c*. Cytochrome *c* unfolds at a much lower temperature in solution.[102] This demonstrates that the folded conformations of a gas-phase protein can be much more stable than in solution. However, the results described above show that Coulomb repulsion destabilizes folded conformations in the gas phase. Figure 9 shows drift time distributions for the +7 charge state of cytochrome *c* measured as a function of the drift tube temperature. The dashed line shows the distribution recorded at room temperature with a high injection energy (2100 eV) while the other distributions were recorded with a low injection energy (350 eV). As the temperature is raised the +7 charge state unfolds, and at 200 °C there is a single, relatively narrow peak at the same position as the smaller peak in the high injection energy distribution (shown by the dashed line). Between 200 and 300 °C a further structural transition occurs and the peak moves to the position of the more unfolded conformation in the high injection energy distribution. These thermal unfolding transitions provide an excellent test of the force fields used in molecular dynamics simulations of proteins.

By introducing a base in the desolvation region it is possible remove protons from highly protonated cytochrome *c* ions and form the low charge states, +3 to +5. These charge states have compact conformations even when they are produced from high charge states that were generated by electrospraying an acidified solution where cytochrome *c* is denatured. The drift

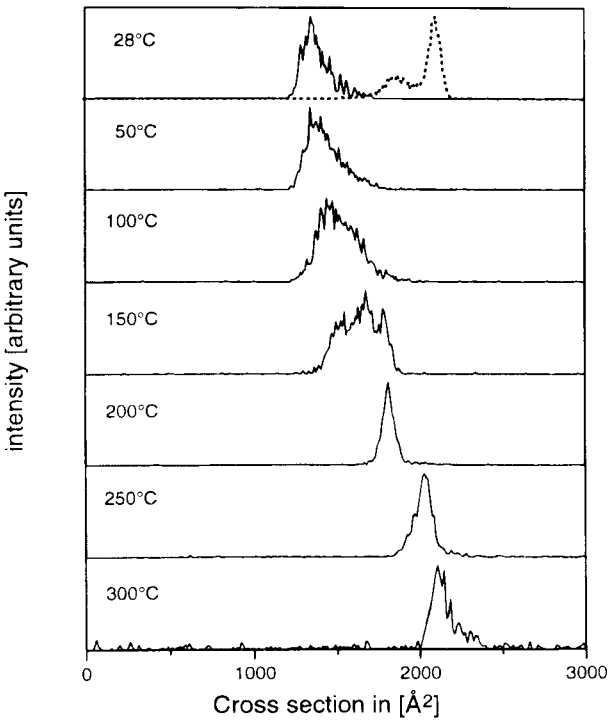

Figure 9. Drift time distributions recorded for the +7 charge state of cytochrome *c* as a function of drift tube temperature. The drift time-scale has been converted into a cross-section scale so that distributions recorded at different temperatures can be easily compared. The dashed line shows the distribution measured at high injection energy (2100 eV). The other distributions were recorded with a low injection energy (350 eV).

time distributions for the high charge states indicate that they are unfolded. Thus the folded conformations observed for the low charge states must result from refolding in the gas phase. The cross-sections for these refolded conformations are similar to the cross-sections for the compact conformations observed for the +6 to +8 charge states from an unacidified solution. However, this should not be taken to indicate that the refolded conformations have the native structure. The native conformation is expected to be stable in the gas phase because it has a large number of hydrogen bonds and van der Waals contacts. However, it is probably not the lowest energy gas-phase conformation. Furthermore, the native conformation is probably not kinetically accessible without a solvent.

Folding processes similar to those described above for cytochrome *c* have also been observed for the low-charge states of apomyoglobin. The +6 charge state of apomyoglobin is particularly noteworthy because it provides a dramatic example of an activation barrier for gas-phase protein folding.[59] Drift time distibutions measured for the +6 charge state of apomyglobin are shown in Fig. 10. The ions were produced by proton stripping of high charge states generated by electrospraying an acidified solution. At low injection energies a partially folded conformation is observed. As the injection energy is raised the distribution shifts to shorter drift times as the protein refolds. The feature observed at low injection energies is more compact than its high charge state precursors and so it is clearly an intermediate in the folding process and there must be an

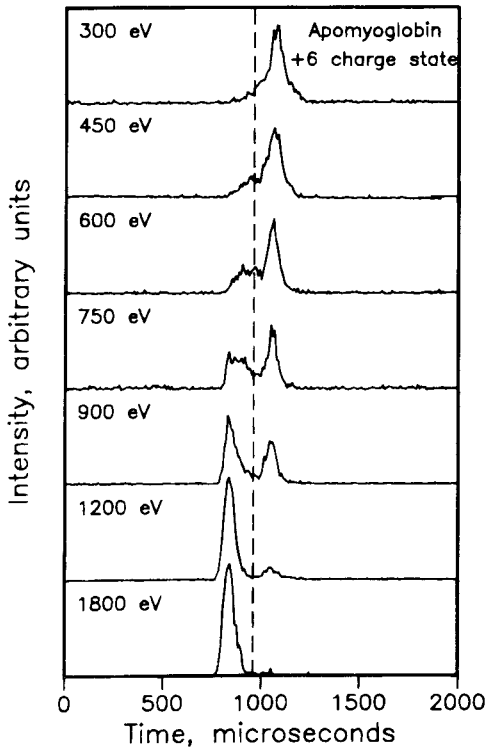

Figure 10. Drift time distributions recorded for the +6 charge state of apomyoglobin as a function of injection energy. The ions were produced by proton stripping higher charge states with a base in the desolvation region. The dashed line shows the drift time expected for the native conformation of myoglobin.

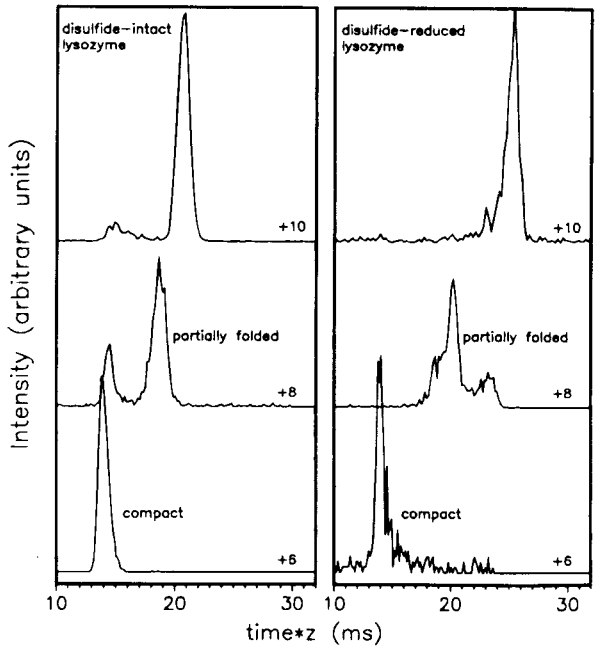

Figure 11. Drift time distributions recorded for the +6, +8 and +10 charge states of lysozyme that were electrosprayed from disulfide-intact (left) and disulfide-reduced (right) solutions. The +8 and +10 disulfide-intact ions were obtained by direct electrospray ionization. All other charge states were obtained by proton stripping higher charge states with a base in the desolvation region.

activation barrier separating the partially folded conformation from the completely refolded conformation. This activation barrier probably results from Coulomb interactions. As the protein folds the Coulomb energy must increase, but this increase is offset by the attractive intramolecular interactions in the compact conformation. However, Coulomb repulsion is a long-range interaction and during the folding process the Coulomb energy will increase before it can be offset by the shorter range intramolecular interactions, leading to a Coulomb barrier to protein folding.

Unfolding transitions induced by Coulomb repulsion, similar to that observed for the intermediate charge states of cytochrome *c*, have also been observed with apomyglobin and ubiquitin. On the other hand, BPTI does not show an unfolding transition. BPTI is a small protein, 58 residues, which has three disulfide bridges that partly lock its three-dimensional structure in place. BPTI is very resistant to thermal, acid and base denaturation. The other three proteins mentioned above, cytochrome *c*, apomyoglobin and ubiquitin, do not contain disulfide bridges and so they are free to adopt unfolded gas-phase conformations as the charge increases. Lysozyme contains four disulfide bridges and drift time distributions have been recorded for this protein in disulfide-intact and disulfide-reduced forms.[103] Elecrospray ionization of the disulfide-intact solution favors low charge states (+8 to +10) whereas the disulfide-reduced solution favors high charge states (+10 to +18). Figure 11 shows drift time distributions for the +6, +8 and +10 charge states of disulfide-intact (left) and disulfide-reduced lysozyme (right).[60]

The disulfide-intact +8 and +10 charge states were obtained by direct electrospray ionization whereas the other charge states were formed by proton stripping reactions in the desolvation region. Both disulfide-reduced and disulfide-intact lysozyme unfold as the charge increases, but the conformations observed for the disulfide-reduced are generally more unfolded than those observed for the disulfide-intact form. For the +6 charge states both disulfide-intact and disulfide-reduced lysozyme have compact folded conformations with essentially the same cross-sections, although this does not necessarily indicate that they have the same conformations.

Electrospray ionization can also be used to produce negatively charged protein ions where the charge results from deprotonation of acidic residues. Comparison of the conformations observed for positively and negatively charged protein ions can provide information about how the location of the charge sites (determined by the numbers and positions of basic and acidic amino acids) affects the gas-phase conformations.[104] For cytochrome *c* positive ions up to +20 can be produced whereas for negative ions the highest charge state observed is −12. This difference can be understood by considering the number of basic and acidic residues. Cytochrome *c* has 22 basic lysine and arginine residues but only 12 acidic asparginine and glutamic acid residues. The basic and acidic residues are approximately equally distributed along the primary sequence. Figure 12 shows cross-sections determined for the largest features observed at high injection energies for the −4 to −12 and +3 to +20 charge states of cytochrome *c*. For the high- and low-charge states, the cross-sections for the negatively charged ions are nearly identical with

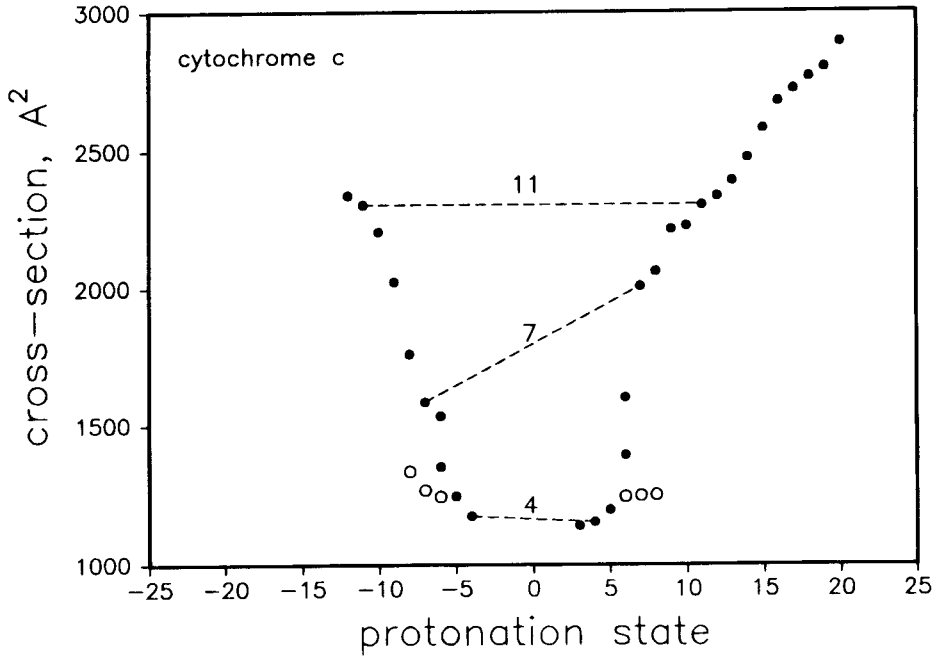

Figure 12. Cross-sections measured for negatively charged (deprotonated) and positively charged (protonated) forms of cytochrome *c*. Only data for the most abundant feature in the drift time distributions recorded at high injection energies are plotted. The dashed lines show that low and high charge states have similar cross-sections. Intermediate charge states such as the ±7 charge states have significantly different cross-sections.

those obtained for their positively charged counterparts. The primary differences are observed for the intermediate charge states where, as discussed above, repulsive Coulombic interactions are comparable to the attractive intramolecular interactions that hold the protein in a folded conformation. For these charge states the location of the charges apparently plays a role in determining which gas-phase conformations dominate the ion mobility distribution. For example, the dominant conformation observed for the −7 charge state is significantly more folded than the dominant conformation observed for the +7 charge state. The unfolding that occurs as the charge state increases is somewhat analogous to acid denaturation of a protein in solution. In solution, the compact native state is stable over a restricted pH range near 7 and as the pH is increased or decreased, it unfolds.[105]

H–D exchange has recently been used to examine peptide[106] and protein ions[39,40,107,108] in the gas phase. The basic assumption behind these studies is that the fraction of exchangeable hydrogens that undergo H–D exchange can provide a measure of the accessible surface area, which in turn can be used to deduce structural information. This information may complement that obtained from ion mobility measurements. Figure 13 shows the results of some H–D exchange studies of the +8 charge state of horse heart cytochrome *c*. Horse heart cytochrome *c* has 198 exchangeable hydrogens, of which 144 are exchanged by the native conformation in a neutral solution. Figure 13 shows drift time distributions and mass spectra measured for the +8 charge state with D_2O introduced into the drift tube.[58] The dashed line shows a portion of the mass spectrum obtained in the absence of D_2O. The plots in the upper half of the figure show results obtained with a low injection energy where the +8 charge state of cytochrome *c* is predominently in compact conformations. The maximum average mass shift observed under these conditions corresponds to the exchange of around 45 hydrogens. The lower half of the figure shows results obtained at a high injection energy where the protein is in a partially unfolded conformation. The mass spectrum indicates an average exchange level of ~60 hydrogens. The higher exchange level observed for the partially folded conformation is in line with expectations. However, the exchange levels are much lower than for the native conformation in solution. Furthermore, the exchange levels for the extended conformations of the +8 to +18 charge states are all

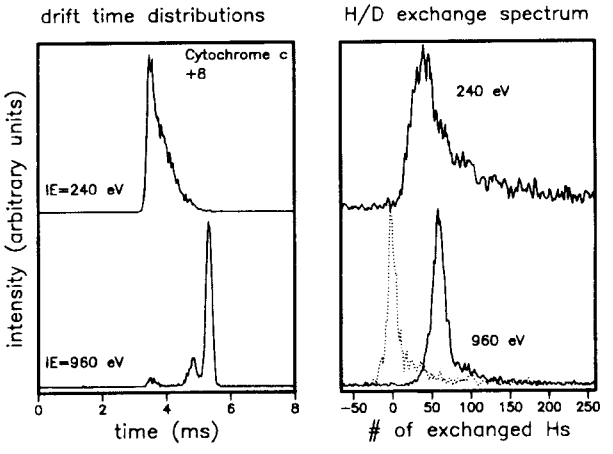

Figure 13. Drift time distributions (left) and mass spectra (right) recorded for the +8 charge state of horse-heart cytochrome *c* using a buffer gas containing 0.3 Torr of D_2O. The data in the upper half of the figure were recorded using an injection energy of 960 eV and those in the lower half with an injection energy of 240 eV. The dashed line shows the mass spectrum recorded without D_2O in the drift tube.

approximately the same, ~60, while the ion mobility measurements show that the average cross-section increases substantially over this range. It appears that the H–D exchange levels are insensitive to subtle changes in conformation for different charge states of cytochrome *c*. The observation that the higher charge states have a constant exchange level is in agreement with previous H–D exchange studies for cytochrome *c* performed by McLafferty and co-workers using Fourier transform ion cyclotron resonance (FT-ICR) spectrometry.[39,40] However, the exchange levels in drift tube experiments were smaller than in the FT-ICR studies.

Studies of gas-phase proteins provide information about the intramolecular interactions that are important in defining their solution-phase conformations. However, gas-phase studies also provide new opportunities to study the solvation effects that also play an important role in determining the conformation in solution. Starting with an unsolvated protein in the gas phase it is in principle possible to hydrate it sequentially and study the hydration process one water molecule at a time. Thermodynamic information can be obtained from equilibrium constant measurements for the hydration reactions. Kebarle and co-workers[109] have examined the hydration of a few small polypeptides. Recently, Woenckhaus and Jarrold[101] have reported measurements of the free energy changes for the adsorption of the first few water molecules on the unfolded +7 charge state of cytochrome *c* and the compact, refolded +5 charge state. The equilibrium constant measurements were performed by adding water vapor to the helium buffer gas. With water vapor pressures of around 1 Torr at room temperature, the mass spectra showed no evidence for water adsorption and it was necessary to cool the drift tube to study the hydration reactions. Free energy changes at 271 K were determined for adsorption of the first nine water molecules on the refolded + 5 charge state and the first five water molecules on the unfolded +7 charge state. The free energy changes are shown in Fig. 14, where they are compared with the free energy changes for the adsorption of the first few water molecules on $GlyH^+$ and H_3O^+.[109,110] Surprisingly, the unfolded conformation (+7 charge state) has smaller initial free energy changes than the refolded conformation (+5 charge state). However, the free energy changes for initial hydration of both the unfolded and refolded conformations of cytochrome *c* are substantially smaller than the free energy changes for initial hydration of H_3O^+ and $GlyH^+$. The free energy changes for the adsorption of the first water molecule on $(Gly)_nH^+$ at 293 K are −41, −37, −28 and −24 kJ mol^{-1} for n = 1–4.[109] The substantial differences in the free energy changes between n = 2 and 3 has been attributed to cyclization of the larger polypeptides through hydrogen bonds to carbonyl oxygens. This intramolecular charge 'solvation' decreases the free energy change for adsorption of the first water molecule by effectively shielding the charge. The small free energy changes for the adsorption of the first few water molecules on to cytochrome *c* indicates that the charge is very effectively shielded, presumably by interactions with a number of carbonyl oxygens. However, it is still not clear why the free energy changes for the unfolded +7 charge state are significantly

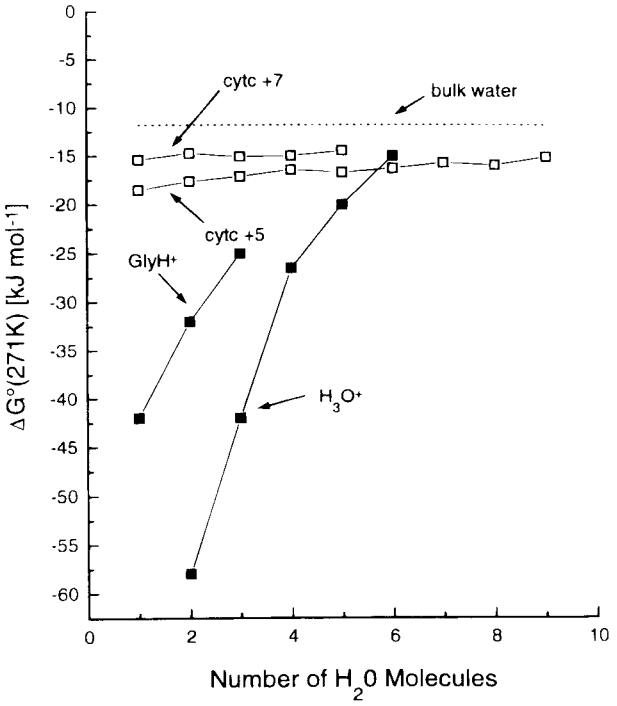

Figure 14. Free energy changes for adsorption of the first few water molecules on the refolded +5 charge state and the unfolded +7 charge state of bovine cytochrome *c*. Free energy changes for adsorption of water on H_3O^+ and $GlyH^+$ are shown for comparison. The dashed line shows the free energy change for adsorption on bulk water.

smaller than those for the compact refolded +5 charge state. This may indicate that the charge is more effectively shielded in the unfolded +7 charge state, or the incorporation of some of the adsorbed water molecules as structural water molecules in the folded +5 charge state.

Oligonucleotides

Because of their electronegative phosphate backbone, DNA and RNA can most readily be electrosprayed from basic solutions to yield negative ions. Figure 15 shows drift time distributions measured for a 10-residue oligonucleotide comprised entirely of thymine bases (T_{10}). Distributions are shown for the −2 to −6 charge states of $[T_{10} - nH^+]^{n-}$, where n is the number of deprotonated sites. There is a sharp unfolding transition between the −3 and −5 charge states which presumably results from Coulomb repulsion. Some typical structures obtained for the T_{10} oligonucleotide using the Insight II molecular modeling software are shown in Fig. 15 for the −2, −4 and −6 charge states. The average cross-sections obtained by sampling a large number of different structures depend on the location of the charges. For the 10-unit homopolymer studied here, which is expected to be deprotonated along the nine phosphodiester linkages, the number of possible combinations of assigning charges to sites is given by 9!/[n!(9 − n)!]. From comparisons of collision cross-sections for modelling results with our experimental data it appears that the transition region is best

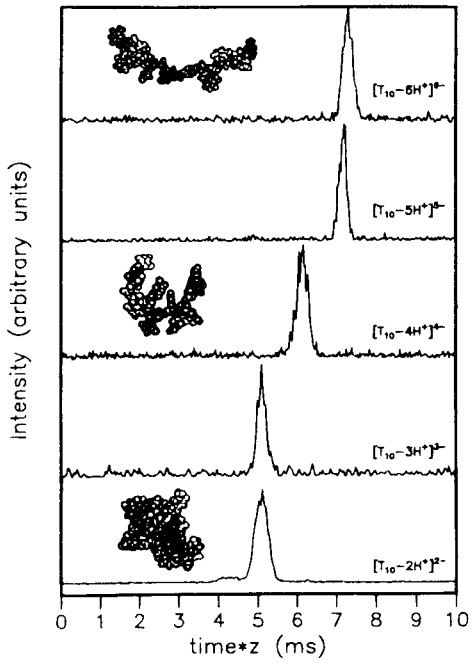

Figure 15. Drift time distributions for the −2 to −6 states of T_{10}. The geometries shown for the −2, −4 and −6 charge states were obtained from Insight II molecular modeling software.

described when deprotonation sites are dispersed along the entire backbone rather than placed on adjacent sites.[111]

FUTURE PROSPECTS

It is clear from the preceding description of some of the recent applications of ion mobility measurements that this area has developed rapidly in the last few years. In particular, the studies of biomolecules have only just begun and ion mobility measurements will be a rich source of information about the conformations, folding and refolding of these species in the next few years. The combination of ion mobility measurements with electrospray ionization essentially removes the limit on the mass of the species that can be studied and so these methods can be extended to even larger biological systems. An effort is currently being made to perform mobility measurements for intact viruses. The order of magnitude improvement in the resolution available from ion mobility measurements has recently revealed many more structural isomers for atomic clusters. High resolution ion mobility measurements for protein ions are currently under way. A further order of magnitude improvement in the resolution is desirable. However, this will be exceedingly difficult to realize simply by extending the current methods, so a new approach must be found if the resolution is to be significantly improved. Ion mobility measurements are basically a separations technique which can be combined with other methods to provide information about the resolved geometries. For example, measurements of the properties of atomic clusters as a function of the number of atoms are not particularly valuable if a distribution of isomers are present. Measurements need to be performed for the individual isomers. This is also true for biomolecules. The first studies along these lines have examined the chemistry of the separated geometries. It would be useful to combine the ion mobility measurements with a spectroscopic technique that would provide structural information. This is desirable because the structural information obtained from a mobility measurement is often ambiguous. However, it is difficult to find a technique that is compatable with low signal intensities available after separation of the different geometries. Photoelectron spectroscopy using a magnetic bottle spectrometer has high sensitivity and efforts are currently under way to record photoelectron spectra for the isomers resolved in the ion mobility measurements.

Acknowledgements

It is a pleasure to acknowledge the invaluable contributions of our colleagues Konstantin Shelimov, Jim Fye, Robert Hudgins, Philippe Dugourd, Alexandre Shvartsburg, Jurgen Woenckhaus, Yi Mao, Steve Valentine, Yansheng Liu, Cherokee Hoagland and Ann Counterman to the work described here. We also gratefully acknowledge the National Science Foundation (CHE-9306900, CHE-9625199 and CHE-97XXXXX) and the Petroleum Research Fund, administered by the American Chemical Society, for support of this work.

REFERENCES

1. B. R. Rowe, D. W. Fahey, F. C. Fehsenfeld and D. L. Albritton, *J. Chem. Phys.* **73**, 194 (1980).
2. D. F. Hagen, *Anal. Chem.* **51**, 870 (1979).
3. M. J. Cohen and F. W. Karasek, *J. Chromatogr. Sci.* **8**, 330 (1970).
4. R. H. St. Louis and H. H. Hill, *Crit. Rev. Anal. Chem.* **21**, 321 (1990).
5. H. H. Hill, W. F. Siems, R. H. St. Louis and D. G. McMinn, *Anal. Chem.* **62**, 1201*A* (1990).
6. Y. H. Chen, H. H. Hill and D. P. Wittmer, *Int. J. Mass Spectrom. Ion Processes* **154**, 1 (1996).
7. K. T. Whitby and W. E. Clark, *Tellus* **18**, 573 (1966).
8. T. M. Sanders and S. R. Forest, *J. Appl. Phys.* **66**, 3317 (1989).
9. Y. Kaneko, M. R. Megill and J. B. Hasted, *J. Chem. Phys.* **45**, 3741 (1966).
10. V. Nestler, B. Betz and P. Warneck, *Ber. Bunsenges. Phys. Chem.* **81**, 13 (1977).
11. R. Thomas, A. Barassin and R. R. Burke, *Int. J. Mass Spectrom. Ion Phys.* **28**, 275 (1978).
12. W. Lindinger, E. Alge, H. Stori, R. N. Varney, H. Helm, P. Holzmann and M. Pahl, *Int. J. Mass Spectrom. Ion Phys.* **30**, 251 (1979).
13. R. Johnsen, M. A. Biondi and M. J. Hatashi, *J. Chem. Phys.* **77**, 2545 (1982).
14. F. Bohringer and F. Arnold, *J. Chem. Phys.* **77**, 5534 (1982).
15. H. Bohringer and F. Arnold, *Int. J. Mass Spectrom. Ion Processes* **49**, 61 (1983).
16. M. F. Jarrold, J. E. Bower and K. Creegan, *J. Chem. Phys.* **90**, 3615 (1989).
17. M. F. Jarrold, *J. Phys. Chem.* **99**, 11 (1995).
18. P. P. Radi, G. von Helden, M. T. Hsu, P. R. Kemper and M. T. Bowers, *Int. J. Mass Spectrom. Ion Processes* **109**, 49 (1991).
19. P. R. Kemper and M. T. Bowers, *J. Phys. Chem.* **95**, 5134 (1991).

20. G. von Helden, M.-T. Hsu, P. R. Kemper and M. T. Bowers, *J. Chem. Phys.* **93**, 3835 (1991).
21. G. von Helden, M.-T. Hsu, N. Gotts and M. T. Bowers, *J. Phys. Chem.* **97**, 8182 (1993).
22. K. B. Shelimov, J. M. Hunter and M. F. Jarrold, *Int. J. Mass Spectrom. Ion Processes* **138**, 17 (1994).
23. J. M. Hunter and M. F. Jarrold, *J. Am. Chem. Soc.* **117**, 103 (1995).
24. M. F. Jarrold and V. A. Constant, *Phys. Rev. Lett.* **67**, 2994 (1992).
25. J. M. Hunter, J. L. Fye, M. F. Jarrold and J. E. Bower, *Phys. Rev. Lett.* **73**, 2063 (1994).
26. M. F. Jarrold and J. E. Bower, *J. Chem. Phys.* **98**, 2399 (1993).
27. D. E. Clemmer, J. M. Hunter, K. B. Shelimov and M. F. Jarrold, *Nature (London)* **372**, 248 (1994).
28. K. B. Shelimov, D. E. Clemmer and M. F. Jarrold, *J. Chem. Soc., Dalton Trans* 567 (1996).
29. G. von Helden, N. G. Gotts, P. Maitre and M. T. Bowers, *Chem. Phys. Lett.* **227**, 601 (1994).
30. J. A. de Gouw, L. N. Ding, M. Krishnamurthy, H. S. Lee, E. B. Anthony, V. M. Bierbaum and S. R. Leone, *J. Chem. Phys.* **105**, 10398 (1996).
31. M. F. Jarrold and E. C. Honea, *J. Am. Chem. Soc.* **114**, 459 (1992).
32. J. M. Hunter, J. L. Fye and M. F. Jarrold, *Science* **260**, 784 (1993).
33. G. von Helden, N. G. Gotts and M. T. Bowers, *Nature (London)* **363**, 60 (1993).
34. Ph. Dugourd, R. R. Hudgins, D. E. Clemmer and M. F. Jarrold, *Rev. Sci. Instrum.* in press.
35. J. J. Monagham, M. Barber, R. Bordolim, E. Sedgewick and A. Taylor, *Org. Mass Spectrom.* **17**, 596 (1982).
36. C. M. Whitehouse, R. N. Dreyer, M. Yamashuta and J. B. Fenn, *Anal. Chem.* **57**, 675 (1985).
37. M. Karas and F. Hillenkamp, *Anal. Chem.* **60**, 2299 (1988).
38. B. E. Winger, K. J. Light-Wahl, A. L. Rockwood and R. D. Smith, *J. Am. Chem. Soc.* **114**, 5897 (1992).
39. D. Suckau, Y. Shi, S. C. Beu, M. W. Senko, J. P. Quinn, F. M. Wampler and F. W. McLafferty, *Proc. Natl. Acad. Sci. USA* **90**, 790 (1993).
40. T. D. Wood, R. A. Chorush, F. M. Wampler, D. P. Little, P. B. O'Connor and F. W. McLafferty, *Proc. Natl. Acad. Sci. USA* **92**, 2451 (1995).
41. D. S. Gross, P. D. Schnier, S. E. Rodriguez-Cruz, C. K. Fagerquist and E. R. Williams, *Proc. Natl. Acad. Sci. USA* **93**, 3143 (1996).
42. P. D. Schnier, D. S. Gross and E. R. Williams, *J. Am. Chem. Soc.* **117**, 6747 (1995).
43. T. R. Covey and D. J. Douglas, *J. Am. Soc. Mass Spectrom.* **4**, 616 (1993).
44. T. R. Covey and D. J. Douglas, *J. Am. Soc. Mass Spectrom.* **4**, 616 (1993).
45. B. A. Collings and D. J. Douglas, *J. Am. Chem. Soc.* **118**, 4488 (1996).
46. K. A. Cox, R. K. Julian, R. G. Cooks and R. E. Kaiser, *J. Am. Soc. Mass Spectrom.* **5**, 127 (1994).
47. A. P. Quist, J. Ahlbom, C. T. Reimann and B. U. R. Sundquist, *Nucl. Instrum. Methods Phys. Res. B* **88**, 164 (1994); P. A. Sullivan, J. Axelsson, S. Altmann, A. P. Quist, B. U. R. Sundquist and C. T. Reinmann, *J. Am. Soc. Mass Spectrom.* **7**, 329 (1996).
48. R. D. Smith, J. A. Loo, R. R. Loo, M. Busman and H. R. Udseth, *Mass Spectrom. Rev.* **10**, 359 (1991).
49. R. D. Smith, J. A. Loo, R. R. Loo and H. R. Udseth, *Mass Spectrom. Rev.* **11**, 434 (1992).
50. D. Wittmer, Y. H. Chen, B. K. Luckenbill and H. H. Hill, *Anal. Chem.* **66**, 2348 (1994).
51. G. von Helden, T. Wyttenbach and M. T. Bowers, *Science* **267**, 1483 (1995).
52. G. von Helden, T. Wyttenbach and M. T. Bowers, *Int. J. Mass. Spectrom. Ion Processes* **146/147**, 349 (1995).
53. T. Wyttenbach, G. von Helden and M. T. Bowers, *J. Am. Chem. Soc.* **118**, 8355 (1996).
54. J. B. Fenn, M. Mann, C. K. Meng, S. F. Wong and C. M. Whitehouse, *Science* **246**, 64 (1989).
55. D. E. Clemmer, R. R. Hudgins and M. F. Jarrold, *J. Am. Chem. Soc.* **117**, 10141 (1995).
56. K. B. Shelimov and M. F. Jarrold, *J. Am. Chem. Soc.* **118**, 10313 (1996).
57. K. B. Shelimov, D. E. Clemmer, R. R. Hudgins and M. F. Jarrold, *J. Am. Chem. Soc.* in press.
58. S. J. Valentine and D. E. Clemmer, *J. Am. Chem Soc.* submitted for publication.
59. K. B. Shelimov and M. F. Jarrold, *J. Am. Chem. Soc.* in press.
60. S. J. Valentine, J. G. Anderson, A. D. Ellington and D. E. Clemmer, *J. Am. Chem. Soc.* submitted for publication.
61. S. J. Valentine and D. E. Clemmer, *J. Am. Soc. Mass Spectrom.* submitted for publication.
62. R. A. Dressler, H. Meyer and S. R. Leone, *J. Chem. Phys.* **87**, 6029 (1987); S. R. Leone, in *Bimolecular Collisions*, edited by M. N. R. Ashford and J. E. Baggott. Royal Society of Chemistry, London, 1989.
63. E. A. Mason and E. W. McDaniel, *Transport Properties of Ions in Gases*. Wiley, New York (1988).
64. H. W. Revercomb and E. A. Mason, *Anal. Chem.* **47**, 970 (1975).
65. F. Howorka, F. C. Fehsenfeld and D. L. Albritton, *J. Phys. B* **12**, 4189 (1979).
66. J. M. Hunter, J. L. Fye, N. M. Boivin and M. F. Jarrold, *J. Phys. Chem.* **98**, 7440 (1994).
67. M. F. Jarrold and J. A. Bower, *J. Chem. Phys.* **96**, 9180 (1992).
68. M. F. Jarrold and E. C. Honea, *J. Phys. Chem.* **95**, 9181 (1991).
69. J. Woenckhaus, Y. Mao and M. F. Jarrold, to be published.
70. S. D. Huang, L. Kolaitis and D. M. Lubman, *Appl. Spectrosc.* **41**, 1371 (1987).
71. Y. H. Chen, H. H. Hill and D. P. Wittmer, *Int. J. Mass Spectrom. Ion Processes* **154**, 1 (1996).
72. N. E. Bradbury and R. A. Nielsen, *Phys. Rev.* **49**, 388 (1936).
73. F. J. Knorr, R. L. Eatherton, W. F. Siems and H. H. Hill, *Anal. Chem.* **57**, 402 (1985).
74. A. A. Shvartsburg, J. Woenckhaus and M. F. Jarrold, to be published.
75. J. O. Hirschfelder, C. F. Curtiss and R. B. Bird, *Molecular Theory of Gases and Liquids*. Wiley, New York (1954).
76. E. Mack, *J. Am. Chem. Soc.* **47**, 2468 (1925).
77. S. Lee, T. Wyttenbach and M. T. Bowers, *J. Am. Chem. Soc.* **117**, 10159 (1995).
78. L. D. Book, C. Xu and G. E. Scuseria, *Chem. Phys. Lett.* **222**, 281 (1994).
79. G. von Helden, M. T. Hsu, N. G. Gotts, P. R. Kemper and M. T. Bowers, *Chem. Phys. Lett.* **204**, 15 (1993).
80. A. A. Shvartsburg and M. F. Jarrold, *Chem. Phys. Lett.* in press.
81. M. F. Mesleh, J. M. Hunter, A. A. Shvatsburg, G. C. Schatz and M. F. Jarrold, *J. Phys. Chem.* in press.
82. S. N. Lin, G. W. Griffin, E. C. Horning and W. E. Wentworth, *J. Chem. Phys.* **60**, 4994 (1974).
83. M. F. Mesleh, G. C. Schatz and M. F. Jarrold, unpublished work.
84. M. D. Wessel and P. C. Jurs, *Anal. Chem.* **66**, 2480 (1994).
85. K. S. Pitzer and E. Clementi, *J. Am. Chem. Soc.* **81**, 4477 (1959); R. Hoffmann, *Tetrahedron* **22**, 521 (1966); S. W. McElvaney, B. I. Dunlap and A. O'Keefe, *J. Chem. Phys.* **86**, 715 (1987).
86. J. M. Hunter, J. L. Fye, E. J. Roskamp and M. F. Jarrold, *J. Phys. Chem.* **98**, 1810 (1994).
87. N. S. Goroff, *Acc. Chem. Res.* **29**, 77 (1996).
88. For a recent review, see D. S. Bethune, R. D. Johnson, J. R. Salem, M. S. de Vries and C. S. Yannoni, *Nature (London)* **366**, 123 (1993).
89. N. G. Gotts, G. von Helden and M. T. Bowers, *Int. J. Mass Spectrom. Ion Processes* **149/150**, 217 (1995).
90. Ph. Dugourd, R. R. Hudgins and M. F. Jarrold, to be published.
91. J. E. Campana, T. M. Barlak, R. J. Colton, J. J. Decorpo, J. R. Wyatt and B. I. Dunlap, *Phys. Rev. Lett.* **47**, 1046 (1981).
92. R. Pflaum, P. Pfau, K. Sattler and E. Recknagel, *Surf. Sci.* **156**, 165 (1985).
93. E. C. Honea, M. L. Homer, P. Labastie and R. L. Whetten, *Phys. Rev. Lett.* **63**, 394 (1989).
94. Y. J. Twu, C. W. S. Conover, Y. A. Yang and L. A. Bloomfield, *Phys. Rev. B* **42**, 5306 (1990).

95. P. Dugourd, R. R. Hudgins and M. F. Jarrold, *Chem. Phys. Lett.* in press.
96. P. Dougourd, R. R. Hudgins, J. Tenenbaum and M. F. Jarrold, *Phys. Rev. Lett.* submitted for publication.
97. G. W. Bushnell, G. V. Louie and G. D. Brayer, *J. Mol. Biol.* **214**, 585 (1990).
98. P. X. Qi, D. L. DiStefano and A. J. Wand, *Biochemistry* **33**, 6408 (1994).
99. W. F. van Gunsteren and M. Karplus, *Biochemistry* **21**, 2259 (1982).
100. M. Levitt and R. Sharon, *Proc. Natl. Acad. Sci. USA* **85**, 7557 (1988).
101. J. Woenckhaus and M. F. Jarrold, to be published.
102. T. Y. Tsong, *Biochemistry* **12**, 2209 (1973).
103. J. A. Loo, C. G. Edmonds, H. R. Udseth and R. D. Smith, *Anal. Chem.* **62**, 693 (1990).
104. Y. Liu, S. J. Valentine and D. E. Clemmer, to be published.
105. For recent discussions of the stabilities of proteins as a function of pH, see A.-S. Yang and B. Honig, *J. Mol. Biol.* **231**, 459 (1993); D. Stigter, D. O. V. Alonso and K. A. Dill, *Proc. Natl. Acad. Sci. USA* **88**, 4176 (1991), and references cited therein.
106. For a more complete discussion, see S. Campbell, M. T. Rodgers, E. M. Marzluff and J. L. Beauchamp, *J. Am. Chem. Soc.* **117**, 12840 (1995); and references cited therein.
107. B. E. Winger, K. J. Light-Wahl, A. L. Rockwood and R. D. Smith, *J. Am. Chem. Soc.* **114**, 5897 (1992).
108. C. J. Cassady and S. R. Carr, *J. Mass Spectrom.* **31**, 247 (1996).
109. J. S. Klassen, A. T. Blades and P. Kebarle, *J. Phys. Chem.* **99**, 15509 (1995).
110. Y. K. Lau, S. Ikuta and P. Kebarle, *J. Am. Chem. Soc.* **104**, 1462 (1986).
111. C. S. Hoaglund, Y. Liu, A. E. Ellington, M. Pagel and D. E. Clemmer, submitted for publication.